J. Meas. Sci. Instrum., 2024, 15(4): 477-489.
DOI: 10.62756/jmsi.1674-8042.2024048
http://jmsi.publish.founderss.cn/
jmsi@nuc.edu.cn

# Dehazing algorithm for adaptively corrected transmission under multi-scale morphology

ZHANG Shuai, YANG Yan*

*School of Electronic and Information Engineering, Lanzhou Jiaotong University, Lanzhou 730070, China*

***Corresponding author:** YANG Yan (yangyantd@mail.lzjtu.cn)

**Received:** May 15, 2023 **Revised:** July 3, 2023 **Accepted:** August 21, 2023

**Abstract:** In order to solve the problems of color bias and visual deviation caused by inaccurate estimation of transmittance and atmospheric light in image defogging, a new algorithm based on multi-scale morphological reconstruction with adaptive transmittance and atmospheric light correction was proposed. Firstly, the algorithm used the open operation under morphological reconstruction to replace the minimum filter operation in the dark channel, and used the morphological edge to set the scale of the open operation structure elements, and constructed a multi-scale open operation fusion dark channel. After morphological noise reduction, the exact initial transmittance was obtained. According to the relationship between brightness and saturation difference and transmittance, an adaptive transmittance correction model was fitted with Gaussian function to correct the initial transmittance of the sky fog map. Then the local atmospheric light was improved according to the image brightness information and morphology closure operation. Finally, the proposed algorithm was combined with the atmospheric scattering model to obtain an accurate fog free image. The experimental results showed that the proposed algorithm was suitable for fog image restoration under various scenes, the restoration effect was good, and the brightness was suitable.

**Key words:** image dehazing; morphological reconfiguration; multi-scale fusion dark channel; adaptive correction; multi-scene recovery

## 0 Introduction

Outdoor images acquired under hazy weather conditions will be seriously degraded because the air contains a large amount of dust, water droplets, and other suspended particles that make it difficult to obtain the contrast, color, and resolution under the real scenes. Furthermore, applications for outdoor monitoring and inspection systems (e.g., aerospace photography, traffic video screen monitoring, topographic surveys) require accurate image information features, and hazy images will prevent them from obtaining accurate measurement data. Therefore, the study of effective dehazing algorithms is a topic of great practical value.

Nowadays, with the development of domestic and international research, the dehazing methods can be broadly classified into three categories: image enhancement, restoration, and neural networks. The methods based on enhancement[1,2] are a relatively early approach. Although this method can be dehazed to some extent, it does not take into account the nature of image degradation.

Image restoration is a traditional method in the field of fog removal. This series of methods are mainly based on the atmospheric scattering model for the dehazing process. The degraded nature of the image and the prior knowledge are used to estimate the parameters, thus completing the clarification of the haze image. By studying the dark channel prior (DCP) de-fogging algorithm of a large number of haze images[3], they found that the dark channel value of most haze images tend to 0. Indirectly, the atmospheric scattering model is reduced by using the elimination method to solve for the haze-free images. However, this method has serious color distortion in the sky region of the haze image, because the dark channel value of the sky region does not tend to be 0. Zhu et al.[4] proposed a color attenuation prior (CAP) to recover the scene depth of the hazy image based on a linear model. Although this method can recover more detailed information, its atmospheric scattering coefficients are selected singly. Moreover, the method leads to an overestimation of the transmission, which tends to produce incomplete dehazing. Wang et al.[5] found that the pixel degradation process of haze images was related to the distance of light acquired by the acquisition device. They proposed a dehazing algorithm based on linear transmission, but the saturation of the haze-free image

obtained by this method is high. Yang et al.[6] designed a dehazing algorithm that used a segmentation function instead of the minimum filtering operation in the DCP. Although this algorithm avoids the halo effect in the recovery results, it leaves a residual haze and over-sharpening.

In recent years, there are more and more algorithms based on convolutional neural networks (CNN) for dehazing[7-10]. CNN-based dehazing algorithms are classified into two main categories. The first category is a non-end-to-end approach that uses neural networks to estimate the parameters. The other is the end-to-end dehazing network, which can directly output haze-free images. Li et al.[7] proposed an integrated all-in-one dehazing network (AOD-Net), which was trained by integrating atmospheric light and transmission into a single parameter to obtain hazy-free images. Ren et al.[9] developed a multi-scale convolutional neural network (MSCNN) model to learn the mapping relationship between haze images and transmission. Zheng et al.[10] proposed a multi-guided bilateral network (MGB-Net) for image dehazing, which could affine high-quality features of images as a way to achieve the purpose of dehazing. It is worth noting that these methods lack a large number of real haze images for training and mainly use synthetic images, which leads to unstable dehazing effects.

An adaptive transmission correction dehazing algorithm under multi-scale morphology was proposed. First, a multi-scale fused opening dark channel (MFODC) was constructed based on morphological reconstruction. Then, according to the CAP and Gaussian decay mapping, the adaptive transmission correction function was obtained through the connection of lightness, saturation, and transmission. Finally, morphological closing and atmospheric light adaptive correction formula were combined to improve the local atmospheric light. Experimental results showed that the proposed algorithm achieved relatively satisfactory haze removal in many different haze scenes.

## 1 Related work

### 1.1 Atmospheric scattering model

In the field of computer vision, the atmospheric scattering model is usually used to describe the hazy image formation process, and the mathematical model can be expressed as

$$\boldsymbol{I}(x)=\boldsymbol{J}(x)\boldsymbol{t}(x)+\boldsymbol{A}(x)(1-\boldsymbol{t}(x)), \tag{1}$$

where $x$ indicates the pixel index; $\boldsymbol{I}(x)$ indicates a hazy image acquired in the hazy scene; $\boldsymbol{J}(x)$ is the desired hazy-free image; $\boldsymbol{A}(x)$ denotes the atmospheric light; $\boldsymbol{t}(x)$ denotes the transmission.

The hazy-free image can be recovered by estimating $\boldsymbol{t}(x)$ and $\boldsymbol{A}(x)$. It is worth mentioning that when the medium particles in the air are uniformly distributed, $\boldsymbol{t}(x)$ can be expressed as

$$\boldsymbol{t}(x)=\mathrm{e}^{-\beta \boldsymbol{d}(x)},\ 0\leqslant \boldsymbol{t}(x)\leqslant 1, \tag{2}$$

where $\beta$ is the atmospheric scattering coefficient, and $\boldsymbol{d}(x)$ is the scene depth.

### 1.2 Dark channel prior

He et al.[3] proposed the dark channel prior (DCP) by statistical observation of a large number of clear outdoor images. According to the DCP, in most areas of non-sky regions, some pixels tend to be 0 at least one color channel in the local region, that is

$$\boldsymbol{J}^{\mathrm{dark}}(x)=\min_{y\in\boldsymbol{\Omega}(x)}\left(\min_{c}\boldsymbol{J}^{c}(y)\right)\to 0, \tag{3}$$

where $\boldsymbol{J}^{\mathrm{dark}}(x)$ denotes the dark channel of the hazy-free image; $\boldsymbol{\Omega}(x)$ represents the filter size for the minimum filtering operation and $c$ represents the RGB channels.

Assuming that the atmospheric light $\boldsymbol{A}(x)$ is known, dark channel operation are performed on both sides of Eq. (1) simultaneously, then

$$\frac{\boldsymbol{I}^{\mathrm{dark}}(x)}{\boldsymbol{A}(x)}=\frac{\boldsymbol{J}^{\mathrm{dark}}(x)}{\boldsymbol{A}(x)}\boldsymbol{t}(x)+1-\boldsymbol{t}(x), \tag{4}$$

where $\boldsymbol{I}^{\mathrm{dark}}(x)$ denotes the dark channel of the hazy image. Combining with Eq. (3), the transmission expression is

$$\boldsymbol{t}(x)=1-\frac{\boldsymbol{I}^{\mathrm{dark}}(x)}{\boldsymbol{A}(x)}. \tag{5}$$

According to the atmospheric scattering model, the hazy-free image $\boldsymbol{J}(x)$ can be obtained by

$$\boldsymbol{J}(x)=\frac{\boldsymbol{I}(x)-\boldsymbol{A}(x)}{\max(\boldsymbol{t}(x),\boldsymbol{t}_0(x))}+\boldsymbol{A}(x), \tag{6}$$

where $\boldsymbol{t}_0(x)$ denotes the lower limit of transmission, which prevents $\boldsymbol{t}(x)$ from converging to 0.

## 2 Proposed method

Currently, most of the hazy removal algorithms based on image restoration use the DCP to estimates the transmission. However, the traditional methods based on dark channel prior often produce color distortion and halo effect in the sky area. It is caused by the failure of the minimum filter and the dark channel in the sky area.

To solve these problems, an adaptive transmission correction dehazing algorithm was proposed under morphological operations, which used the morphological opening after reconstruction instead of minimum filtering.

In addition, for the problem of inaccurate estimation of transmission in the sky region, the correction parameters were set to construct an adaptive transmission correction model, which makes the proposed algorithm applicable to image dehazing in different scenes. The specific algorithm flow is shown in Fig.1.

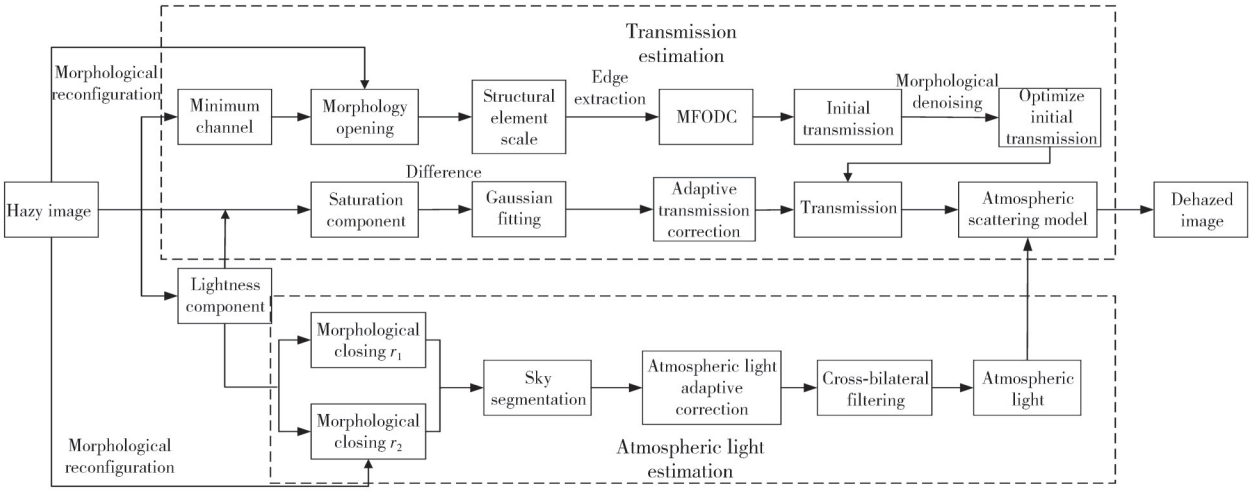


**Fig. 1 Flowchart of proposed algorithm**

## 2.1 Morphological reconstruction

The morphological reconstruction is mainly based on mathematical morphological operations, which is used to simplify the image and preserve the main features of the object shape. We used the concept of morphological opening and morphological closing with geodesic dilation and geodesic erosion to perform the morphological reconstruction.

Let $\boldsymbol{I}$ and $\boldsymbol{g}$ denote the marker image and the template image, and $\boldsymbol{I} \leqslant \boldsymbol{g}$. Then the geodesic dilation is defined as

$$D_g^{(1)}(\boldsymbol{I}) = (\boldsymbol{I} \oplus \boldsymbol{s}) \wedge \boldsymbol{g}, \tag{7}$$

where $\oplus$ denotes the dilation operation; $\boldsymbol{s}$ is the scale of the structural element, and $\wedge$ denotes the smaller value in the corresponding pixel. Thus, the geodesic dilation of dilation number $n$ is

$$D_g^{(n)}(\boldsymbol{I}) = D_g^{(1)}[D_g^{(n-1)}(\boldsymbol{I})]. \tag{8}$$

When $n=0$, $D_g^{(0)}(\boldsymbol{I}) = \boldsymbol{I}$.

Similarly, geodesic erosion is defined as

$$E_g^{(1)}(\boldsymbol{I}) = (\boldsymbol{I} \Theta \boldsymbol{s}) \vee \boldsymbol{g}, \tag{9}$$

where $\Theta$ denotes the erosion operation; $\vee$ denotes the larger value in the corresponding pixel. At this time, $\boldsymbol{I} \geqslant \boldsymbol{g}$, the geodesic erosion of erosion number $n$ is

$$E_g^{(n)}(\boldsymbol{I}) = E_g^{(1)}[E_g^{(n-1)}(\boldsymbol{I})]. \tag{10}$$

When $n=0$, then $E_g^{(0)}(\boldsymbol{I}) = \boldsymbol{I}$.

Therefore, the expansion and erosion of the labeled image after morphological reconstruction of the template image is expressed as

$$R_g^D(\boldsymbol{I}) = D_g^k(\boldsymbol{I}), \tag{11}$$

$$R_g^E(\boldsymbol{I}) = E_g^k(\boldsymbol{I}), \tag{12}$$

where $k$ is the number of iterations, and the iterative operation stabilizes when $D_g^k(\boldsymbol{I}) = D_g^{k+1}(\boldsymbol{I})$ and $E_g^k(\boldsymbol{I}) = E_g^{k+1}(\boldsymbol{I})$.

In summary, we define a morphological opening and closing by reconstruction.

$$\underset{x \in s}{imopen}\,(\boldsymbol{I}(x)) = R_{I(x)}^D[E^s(\boldsymbol{I}(x))], \tag{13}$$

$$\underset{x \in s}{imclose}\,(\boldsymbol{I}(x)) = R_{I(x)}^E[D^s(\boldsymbol{I}(x))], \tag{14}$$

where $imopen(\cdot)$ and $imclose(\cdot)$ denote the morphological opening and the morphological closing, respectively. Then $\boldsymbol{s}$ is the scale of the structural element.

## 2.2 Multi-scale fused opening dark channel

According to the DCP[3], it is known that the dark channel with hazy images is defined as

$$\boldsymbol{I}^{\text{dark}}(x) = \min_{y \in \boldsymbol{\Omega}(x)} \left( \min_{c} \boldsymbol{I}^c(y) \right). \tag{15}$$

As shown in Fig. 2, when the depth of the scene changes dramatically, the dark region tends to expand along the edge due to the minimum filtering operation in the local region.

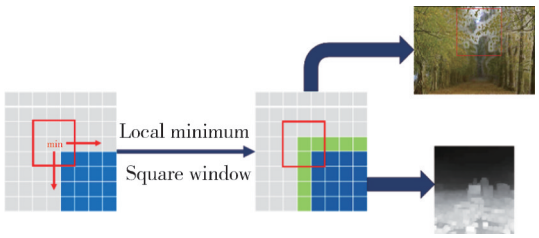


**Fig. 2 Example of minimum filtering operation**

This process results in the halo effect on the recovered haze-free image.

To address this problem, the reconstructed

morphological opening was used instead of the minimum filter. To ensure that the edge region does not expand, the calculation formula is

$$\boldsymbol{I}^{\text{odark}}(x)=\underset{y\in s(x)}{imopen}\left(\min_{c}\boldsymbol{I}^{c}(y)\right), \tag{16}$$

where $\boldsymbol{s}(x)$ is the structural element centered at pixel $x$. The reconstructed morphological opening can continuously consider the image erosion and dilation, effectively counteracting the effect of edge expansion and keeping the edges unchanged.

Fig. 3 shows the comparison of the original dark channel with the opening dark channel and the recovery results. It can be seen that the original dark channel is susceptible to edge coverage, while the edge area of the opening dark channel remains almost unchanged.

(a) Hazy image (b) Original dark channel (c) Opening dark channel (d) Result of (b) (e) Result of (c)

**Fig. 3 Comparison of original dark channel and opening dark channel**

In addition, the selection of the structural element scale is also crucial when applying the opening dark channel. The smaller the structural element scale, the better it can extract the scene structure information in the depth discontinuity region. Thus, the dark channel value at the edge is compensated, and the halo in the edge area is avoided. But it can also oversaturate the hazy-free image. Conversely, a larger proportion of structural element scales contains more dark pixels, which avoids the oversaturation of the image. But the non-edge regions may be affected by the edge pixels at abrupt changes in scene depth, resulting in slight artifacts in the dehazed image at the edge regions. Therefore, a fused opening dark channel (FODC) was used to complement the deficiencies of different structural elements scales.

2.2.1 Morphological edge acquisition

The key to fusion is to construct an effective weight map that is capable of displaying edge regions with depth discontinuity. Therefore, a multi-scale and multi-directional morphological edge detection algorithm is used to extract the edge information of the image as a weight map for the fused opening dark channel[11,12].

**Algorithm 1** Morphological edge acquisition

**Input** Hazy image $\boldsymbol{I}(x)$

**Output** Morphological edge $\boldsymbol{B}_1(x)$

**Step 1** Two different structural element scale morphologies, $3\times3$ decagonal and $5\times5$ rhombic structures, are selected for the morphological opening and closing processing to eliminate noise.

**Step 2** The four-directional structural elements of parallel, perpendicular, positive diagonal, and negative diagonal are selected respectively for morphological edge detection, and four different edge images are obtained.

**Step 3** The information entropy of each edge image is obtained to determine the weight value. These edge images are weighted and calculated based on the ratio of their respective information entropy to the total information entropy. The edge information obtained is defined as $\boldsymbol{B}_1(x)$.

2.2.2 Fused opening dark channel

According to the edge information, the image is divided into the edge region of depth discontinuity and the depth continuity region. Different scales of opening dark channels are selected for the fusion of these two regions, the result of the fusion is defined as the FODC $\boldsymbol{I}_{\text{fuse}}^{\text{odark}}{}_1(x)$, which will be denoted as

$$\boldsymbol{I}_{\text{fuse}}^{\text{odark}}{}_1(x)=\boldsymbol{I}^{\text{odark}1}(x)\times\boldsymbol{B}_1(x)+\boldsymbol{I}^{\text{odark2}}(x)\times(1-\boldsymbol{B}_1(x)), \tag{17}$$

where $\boldsymbol{I}^{\text{odark}1}(x)$ indicates a small-scale opening dark channel in the edge region of the depth discontinuity, and its structure element scale is set as $3\times3$. $\boldsymbol{I}^{\text{odark2}}(x)$ indicates a large-scale opening dark channel in the depth continuity region. And its structure element scale is set as $15\times15$.

Fig. 4 shows the comparison of different scales of opening dark channels and the recovery effects.

Fig. 4(f) shows oversaturation and excessive enhancement in the white window portion. Fig. 4(g) improves the saturation problem, but there are more areas where halo artifacts appear. Fig.4(d) solves these problems effectively by fusing the two with an opening dark channel. But the selected scale may not be applied to all images due to the variable size of the image, which may lead to slight artifacts in the depth edge region of the dehazed image when the size of the image is too large, as shown in the red box in Fig.4(h).

To solve this problem, a multi-scale fused opening dark channel (MFODC) was set. Firstly, the edge information is inflated to obtain the secondary weight map. The

difference operation is done between the secondary weights and the primary weights to derive the expanded region after the inflation, which is defined as the neighborhood of depth edge $B_2(x)$. Then, three different scale open dark channels are constructed by selecting different scale structural elements of depth discontinuous edge region, depth edge neighborhood region, and depth continuity region. Finally, the obtained opening dark channels of different scales are fused. The fused opening dark channel is obtained as

$$I_{\text{fuse}}^{\text{odark}}(x)=\begin{cases} \underset{y\in s_1(x)}{imopen}\left(\min_c I^c(y)\right), & B_1(x)=1,\\ \underset{y\in s_0(x)}{imopen}\left(\min_c I^c(y)\right), & B_2(x)=1,\\ \underset{y\in s_2(x)}{imopen}\left(\min_c I^c(y)\right), & B_1(x)+B_2(x)=0, \end{cases} \tag{18}$$

where $s_0(x)$, $s_1(x)$, and $s_2(x)$ denote the neighborhood of depth edge, the edge region of depth discontinuity, and the depth continuity regions of the structural element scales, respectively. Then, the selection of different structural element scales can be formulated as

$$s_0(x)=\min(\max(s_1(x),\theta),s_2(x)), \tag{19}$$

$$s_2(x)=\max(s_1'(x),\theta), \tag{20}$$

where the structural element scale $s_1(x)$ is set as $3\times 3$; $s_1'(x)$ is used to adjust the structural element scale; $s_2(x)$ in the depth continuity region with the structural element scale is set as $15\times 15$; $\theta$ is used to select the appropriate size adaptively in the neighborhood of depth edge, taken as $\frac{\min(W,H)}{20}$, and $W,H$ are the width and height of the image, respectively.

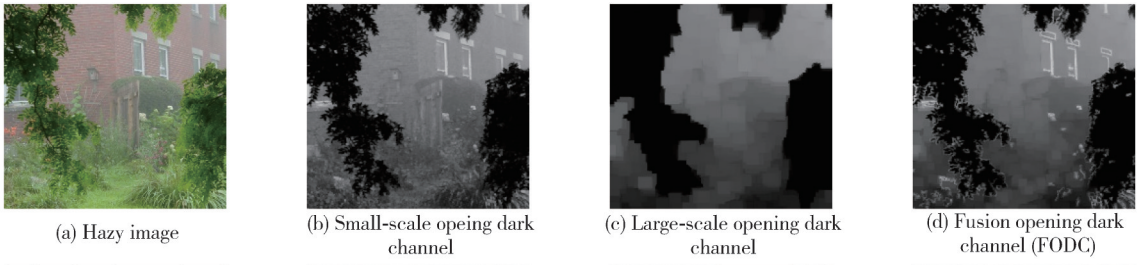

(a) Hazy image (b) Small-scale opeing dark channel (c) Large-scale opening dark channel (d) Fusion opening dark channel (FODC)

(e) Weight map (f) Result of (b) (g) Result of (c) (h) Result of (d)

**Fig. 4 Different scales of opening dark channels and their recovery images**

In summary, we defined the opening dark channels under different structural elements as neighborhood scale, small scale, and large scale opening dark channels. The three opening dark channels are combined to construct MFODC, as shown in Fig.5. The gray part in Fig. 5(b) represents the depth discontinuity edge region $B_1(x)$, and the white part is the neighborhood of the depth edge $B_2(x)$ obtained after inflation.

(a) Edge information inflation (b) Second weight map (c) Neighborhood scale opening dark channel (d) MFODC (e) Result of (d)

**Fig. 5 Multi-scale fused opening dark channel (MFODC)**

## 2.3 Optimized transmission

According to the atmospheric scattering model, assuming that the atmospheric light $A(x)$ is known and combined with the MFODC, a rough initial transmission can be derived as

$$t'(x)=1-\omega\frac{I_{\text{fuse}}^{\text{odark}}(x)}{A(x)}, \tag{21}$$

where $\omega$ represents the adjustment factor, which is used to retain a certain amount of residual hazy and avoid the loss of spatial depth in the image. It is usually taken as 0.95.

Since the hazy image may contain white or highlight

noise to affect the requested initial transmission. To avoid this problem, a noise cancellation method based on morphological operations is used to optimize the rough initial transmission[13,14]. The significance of this method is to extract the information from the noise-containing region of the haze image. Then, the images outside the noise region are processed separately.

The morphological opening and closing are first performed on the rough initial transmission. The morphological closing is used to remove the smaller dark elements above the structural elements of the hazy image. The morphological opening is used to remove white or highlight noise.

$$\boldsymbol{t}_1(x)=\underset{y\in\boldsymbol{s}(x)}{imopen}\left(\underset{y\in\boldsymbol{s}(x)}{imclose}\left(\boldsymbol{t}'(x)\right)\right), \tag{22}$$

$$\boldsymbol{R}(x)=\boldsymbol{t}'(x)-\boldsymbol{t}_1(x), \tag{23}$$

where the structural element scale $\boldsymbol{s}(x)$ is set as $5\times5$, and $\boldsymbol{R}(x)$ denotes the cleared information.

In order to obtain a more accurate initial transmission, it is necessary that the optimized initial transmission has the same range of values as the rough initial transmission. Therefore, the transmission interval of $\boldsymbol{t}_1(x)$ is replaced by the transmission interval of $\boldsymbol{t}'(x)$ to obtain an optimized initial transmission $\boldsymbol{t}(x)$ that not only eliminates the noise interference but also has the same range of values as the rough initial transmission. The specific conversion process can be expressed as

$$\boldsymbol{t}_1'(x)=\boldsymbol{t}_1(x)-\min\left(\boldsymbol{t}_1(x)\right)\times\frac{\max\left(\boldsymbol{t}'(x)\right)-\min\left(\boldsymbol{t}'(x)\right)}{\max\left(\boldsymbol{t}_1(x)\right)-\min\left(\boldsymbol{t}_1(x)\right)}+\min\left(\boldsymbol{t}'(x)\right), \tag{24}$$

$$\boldsymbol{t}(x)=\boldsymbol{t}_1'(x)+\boldsymbol{R}(x). \tag{25}$$

Fig.6 shows the recovery results of the optimized initial transmission.

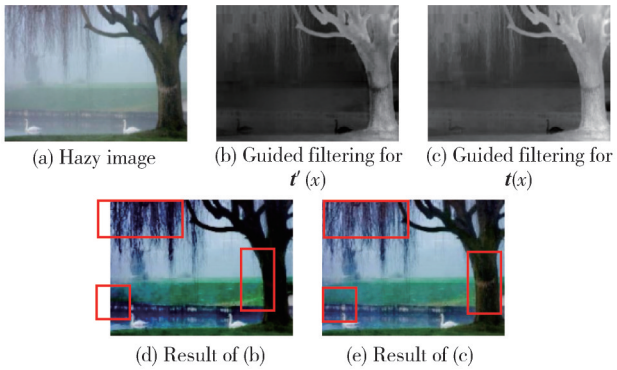


**Fig. 6 Optimized transmission and its recovery results**

In order to clarify the recovery effect objectively, the recovery effect of rough initial transmission was compared with that of optimized initial transmission. As can be seen in Fig. 6(b) and 6(d), the presence of the "white goose" affects the estimation of the transmission, which leads to color distortion in the dehazed image. Fig. 6(c) and 6(e) show that the morphological noise cancellation process eliminates the effect of "white goose" on the estimation of transmission, and the recovered results are closer to the real effect.

## 2.4 Adaptive transmission correction

When the haze image contains the sky area, the dark channel value does not tend to be 0, leading to a serious bias in the estimation of transmission. In this case, the transmission of the sky area needs to be corrected.

The purpose of the lower limit setting in Eq. (6) is to avoid the transmission from approximating to be 0, but it was not considered to avoid the problem of underestimation of the transmission. Therefore, an adaptive transmission constraint lower limit was proposed for the adaptive correction of transmission.

According to the CAP[4], as the scene depth changes, the hazy concentration increases, and the difference between saturation and lightness becomes larger. It can be understood that the scene depth is positively correlated with the hazy concentration and the difference between lightness and saturation. The relationship equation is

$$\boldsymbol{d}(x)\propto\boldsymbol{c}(x)\propto\boldsymbol{V}(x)-\boldsymbol{S}(x), \tag{26}$$

where $\boldsymbol{d}(x)$ denotes the scene depth; $\boldsymbol{c}(x)$ denotes the hazy concentration; $\boldsymbol{V}(x)$ denotes the lightness; and $\boldsymbol{S}(x)$ denotes the saturation.

Fig.7 selects a screenshot of the regions at three different scene depths of a hazy image, and extracts the lightness, saturation, and differences between the three regions.

As can be seen in Fig. 7, the differences in lightness and saturation in the distant sky region is the largest compared to the other regions. According to Eqs. (2) and (26), the scene depth is inversely proportional to the transmission and positively proportional to the difference in lightness and saturation. Therefore, it is assumed that the transmission has a certain attenuation relationship with the difference of brightness and saturation.

Because the Gaussian function has good distribution properties, the shape of the function can be made controllable by adjusting the variance. Therefore, a Gaussian function was used to construct the transmission correction parameter, which controls the degree of dehazing and corrects the transmission of the sky region. The correction parameter is defined as

$$\boldsymbol{t}_0(x)=\exp\left(-\left\{\left[1-\left(\boldsymbol{V}(x)-\boldsymbol{S}(x)\right)\right]^2/\sigma^2\right\}\right), \tag{27}$$

where $\sigma$ is the standard deviation, which usually takes the value of [0,1].

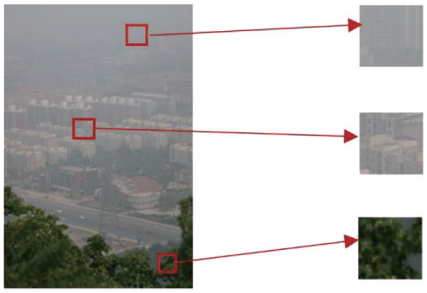

(a) Screenshots of different areas under depth scenes

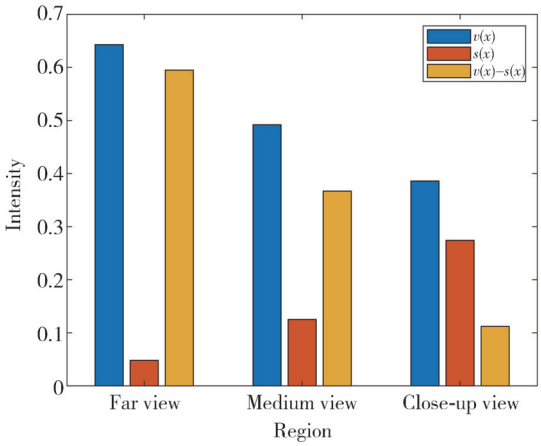


(b) Relationship among lightness, saturation, and scene depth

**Fig. 7 Concentration of haze is positively correlated with difference between the brightness and saturation**

Fig.8 shows the correction of the transmission and the recovery effect under different $\sigma$ values. It can be seen that when the value of $\sigma$ is larger, the corrected transmission will have a serious deviation, and the hazy feeling in the sky and other scene depth areas is obvious. When the value of $\sigma$ is small, the transmission can be effectively corrected. However, if it is too low, the transmission will be corrected too much, and the image after fog removal will appear color distortion.

As shown in Fig. 8(b)—8(e), the recovery effect varies greatly under different hazy images with the same $\sigma$ value. Therefore, it is necessary to set an adaptive $\sigma$, which adaptively selects a suitable $\sigma$ for transmission compensation when processing different hazy images.

Fig.9 shows the Gaussian variation curve of Eq. (27) and the correction for transmission. Since the scene depth is positively correlated with the difference of lightness and saturation. Therefore, the horizontal coordinate of Fig.9 can be approximated as the change of scene depth. By observing Fig.9, it is found that for the far view region, the Gaussian curve of Eq. (27) decreases more slowly and the smoothing effect is more obvious when the value of $\sigma$ is larger. While for the close-up view region, the Gaussian curve of Eq. (27) decreases faster and the smoothing effect is worse compared to the far view region when the value of $\sigma$ is smaller. It can be concluded that the value of $\sigma$ suitable for correcting the transmission is related to the scene depth.

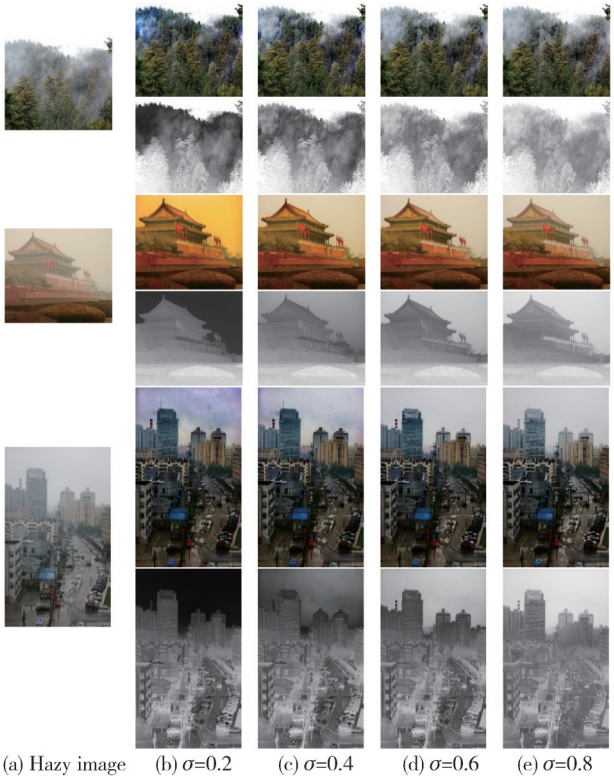

(a) Hazy image (b) $\sigma$=0.2 (c) $\sigma$=0.4 (d) $\sigma$=0.6 (e) $\sigma$=0.8

**Fig. 8 Comparison of recovery results with different transmission and values of $\sigma$**

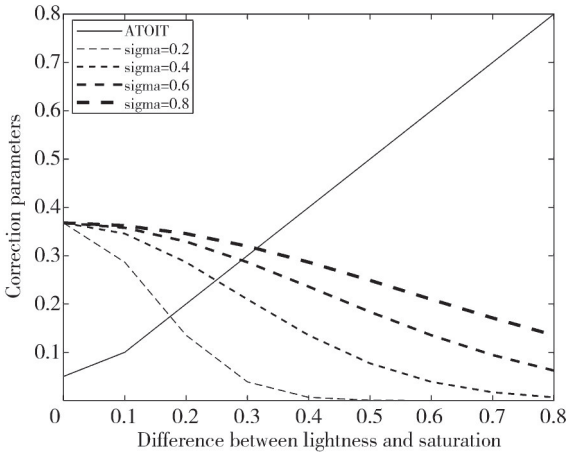


**Fig. 9 Transmission correction curves**

The approximate transformation of initial transmission $t(x)$ (ATOIT) is fitted using the solid line in Fig. 9. Because the lower limit of transmission and correction parameters cannot be 0, the linear region of 0—0.1 is mapped to 0.05—0.1. The intersection points in the figure represent the best correction parameters obtained for different values of $\sigma$.

Therefore, an adaptive $\sigma$ was chosen based on the characteristics of this Gaussian function that varied

according to the scene depth. Observing the grayscale variation of the hazy image, it could be found that the pixel point distribution in the dense hazy region (far view) was at a higher grayscale level compared to the thin hazy or hazy-free region (close-up view). While the maximum channel map of the hazy image containing the sky area happens to have a higher grayscale value in the dense hazy region than in the thin hazy or hazy-free region. Based on this feature, the maximum channel of the hazy image is used as the adaptive $\sigma$. Ensure consistency in local areas and avoid discontinuities when transitioning from close to distant. The maximum channel is applied using the morphological closing to eliminate the gradient between neighbors to obtain the mixing channel $\boldsymbol{I}^{\text{mix}}$, which will be denoted as

$$\boldsymbol{I}^{\text{mix}} = \underset{y\in \boldsymbol{s}_3(x)}{imclose}\left(\max_c \boldsymbol{I}^c(y)\right), \tag{28}$$

where $\boldsymbol{s}_3(x)$ chooses a square element with a structure scale of $15\times 15$. This is because the large scale filter kernel contains more dark pixels to eliminate the effect of white objects.

The joint bilateral filtering is used to refine the mixing channel, and the refinement result is defined as

$$\boldsymbol{\sigma}(x)=\frac{1}{W_x^{jb}}\sum_{y\in \boldsymbol{s}} G_{\sigma_y}\left[\left\| \boldsymbol{I}^{\text{mix}}(x)-\max_c \boldsymbol{I}^c(y)\right\|\right]\cdot G_{\sigma_s}(\|x-y\|)\left[1-\max_c \boldsymbol{I}^c(y)\right], \tag{29}$$

$$W_x^{jb}=\sum_{y\in \boldsymbol{s}} G_{\sigma_y}\left[\left\| \boldsymbol{I}^{\text{mix}}(x)-\max_c \boldsymbol{I}^c(y)\right\|\right] G_{\sigma_s}(\|x-y\|), \tag{30}$$

where $G_{\sigma_y}$, $G_{\sigma_s}$ are Gaussian functions; $W_x^{jb}$ is the normalization factor. $\|\ \|$ denotes the mapping from a linear fugitive space to a non-negative real number.

Therefore, the correction model of transmission can be expressed as

$$\max(\boldsymbol{t}(x),\boldsymbol{t}_0(x))=\max(\boldsymbol{t}(x),\exp\left(-\left\{\left[1-(\boldsymbol{V}(x)-\boldsymbol{S}(x))\right]^2/\boldsymbol{\sigma}(x)^2\right\}\right). \tag{31}$$

## 2.5 Atmospheric light

The atmospheric light $\boldsymbol{A}(x)$ is another important parameter in the dehazing problem, because the selection of atmospheric light determines the visual effect of the dehazed image. When the atmospheric light estimation is high, the result will be too dark. When the atmospheric light estimation is low, the result will be too bright.

Sun et al.[15] proposed a method for local atmospheric light from the local information of the image, which attenuates the impact of atmospheric light estimation from global information by performing morphological closing on the three channels maximum of the hazy image. However, the method also has certain problems. On the one hand, the atmospheric light responds to the lightness information of the image, which is not taken into account by the method from the three channels maximum. On the other hand, when the structural elements scale for morphological closing is chosen too small, it can cause a partial loss of information. Conversely, it will contain useless noise. In addition, when the hazy image contains the sky area, the selection of atmospheric light should be selected in the sky area as much as possible. To address these issues, we made improvements to the Sun et al. algorithm.

### 2.5.1 Atmospheric light estimation

**Algorithm 2** Atmospheric light estimation

**Input** Hazy image $\boldsymbol{I}(x)$

**Output** Atmospheric light $\boldsymbol{A}(x)$

**Step 1** Transfer the hazy image $\boldsymbol{I}(x)$ from RGB color space to HSV color space and extract its lightness component $\boldsymbol{V}(x)$.

**Step 2** The morphological closing is performed on $\boldsymbol{V}(x)$ to eliminate the internal highlighting details. After several experiments, the structural element scales of $r_1=\dfrac{\min(W,H)}{5}$ and $r_2=\dfrac{\min(W,H)}{25}$ are selected to perform morphological closing on $\boldsymbol{V}(x)$. The processing results of the two morphological closing operations are recorded as $\boldsymbol{A}_1(x)$ and $\boldsymbol{A}_2(x)$. Then, the average of $\boldsymbol{A}_1(x)$ and $\boldsymbol{A}_2(x)$ (i. e., $\boldsymbol{A}_{\text{mean}}(x)$) is obtained, expressed as the result of the morphological closing after equalization.

**Step 3** Analysis is performed using the histogram of the requested transmission. If 95% of the pixel values are less than 0.5, the image is judged to contain a sky region[16]. The binary image is obtained by threshold segmentation of the haze image with sky region, and the sky region is marked as $\boldsymbol{I}_{\text{sky}}$.

**Step 4** The ratio of the number of pixels in the sky area of the hazy image account for the number of pixels in the total image is calculated. Then the atmospheric light adaptive correction formula[17] is used to make the atmospheric light take the value in the exact range of the finding. In addition, in order to avoid the influence of the region containing the light source on the atmospheric light seeking, the maximum reflection prior is used to refine the atmospheric light value.

$$\boldsymbol{A}(x)=\begin{cases}(1-\alpha/3)\boldsymbol{A}_{\text{mean}}(x), & x\in \text{NLSR},\\ \max_c \boldsymbol{I}^c(x)/\boldsymbol{t}(x), & x\in \text{LSR},\end{cases} \tag{32}$$

where $\alpha$ denotes the ratio of pixels in the sky area account the total image; NLSR indicates non-light source region;

LSR indicates light source region.

The atmospheric light obtained in both cases of NLSR and LSR in Eq. (32) is fused according to the distribution probability of the light source area[18] to find the exact atmospheric light. The distribution probability of the light source area $P$ can be expressed as

$$P=\left\| \max_c \boldsymbol{I}^c(x)-\min_c \boldsymbol{I}^c(x) \right\|^{\kappa}\begin{cases}<N_{\text{threshold}}, & x\in\text{NLSR},\\ \geqslant N_{\text{threshold}}, & x\in\text{LSR},\end{cases} \tag{33}$$

where $\kappa$ is taken as 2.0 to indicate the adjustment factor for channel differences; $N_{\text{threshold}}$ is taken as 0.07 to indicate the segmentation threshold between light source and non-light source regions (corresponding to a pixel value of 17.85). When the $P$ is less than the threshold $N_{\text{threshold}}$, it is determined that the hazy image does not contain the light source area. Conversely, when the $P$ is greater than the threshold $N_{\text{threshold}}$, it is determined that the hazy image contains the light source region.

**Step 5** The optimized atmospheric light $\boldsymbol{A}(x)$ is obtained by smoothing it with cross bilateral filtering.

The comparison of atmospheric light and recover results are shown as Fig.10.

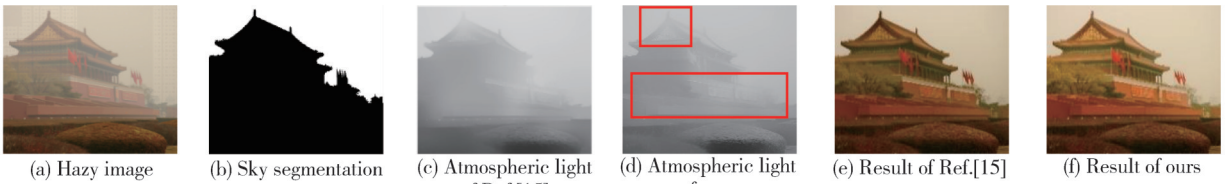

(a) Hazy image (b) Sky segmentation (c) Atmospheric light of Ref.[15] (d) Atmospheric light of ours (e) Result of Ref.[15] (f) Result of ours

**Fig. 10 Comparison of atmospheric light and recovery results**

## 3 Experiment

In order to verify the feasibility of the proposed algorithm, five sets of real hazy images in different scenarios were selected, and they were compared with some classical algorithms from subjective and objective aspects. In addition, for the current emerging deep learning methods in the field of dehazing, three RESIDE synthetic datasets were chosen for algorithm validation[19,20]. The experimental environment is Matlab (R2018a), the hardware environment is Intel(R) Core(TM) i7-10510U CPU@1.80 GHz, 2.30 GHz, and the running system is Windows 11.

### 3.1 Subjective comparison of dehazing effects of different algorithms

We selected 10 images in different scene environments, which were close-up view region scene, far view region scene, abrupt changes in scene depth scene, dense hazy scene, and thin hazy scene images. The recovery results are compared with those of He's algorithm[3], Wang's algorithm[5], Yang's algorithm[6], Sun's algorithm[15], Li's algorithm[8], and Ren's algorithm[9]. It is worth noting that the first four algorithms are based on image restoration, while the last two are data-driven methods based on deep learning. Fig.11 shows the scene image of the close-up view region. It can be seen that He's algorithm and Wang's algorithm can recover many details of the image better when processing the close-up view image. But the contrast of the recovery result of He's algorithm is too high, which causes the image to be too bright. The contrast of the recovery result of Wang's algorithm is too low, which causes the recovery result to be dark. Yang's algorithm and Sun's algorithm have a slight color bias phenomenon on the dehazed image. Li's algorithm has the phenomenon of incomplete dehaze, and the recovery result of Ren's algorithm has the phenomenon of color distortion.

(a) Hazy image (b) He[3] (c) Wang[5] (d) Yang[6] (e) Sun[15] (f) Li[8] (g) Ren[9] (h) Ours

**Fig. 11 Comparison of results of close-up view scene images**

Fig.12 shows the scene image of the far view region. It can be seen that He's algorithm leads to a halo effect at the edge of the alternating far and close-up view, and color distortion in the far view region containing the sky area. Wang's algorithm also shows a color bias in this group of images and the phenomenon of incomplete

dehazing in the far view region. Due to the presence of strong light sources, Yang's algorithm and Sun's algorithm misestimate the atmospheric light and make the overall recovery result too dark or bright. Li's algorithm is better in processing such images, but the saturation is too high, making the recovery result similarly dark. Ren's algorithm maintains a good close-up view but shows a color shift in the far view.

(a) Hazy image (b) He[3] (c) Wang[5] (d) Yang[6] (e) Sun[15] (f) Li[8] (g) Ren[9] (h) Ours

**Fig. 12 Comparison of results of far view scene images**

Fig. 13 shows the image of the scene with abrupt changes in scene depth. It can be seen that He's algorithm and Sun's algorithm also produce a halo effect at the alternating scene depth. Wang's algorithm and Yang's algorithm both show different degrees of incomplete dehazing due to the drastic changes in scene depth. Li's algorithm shows oversaturation in the close-up view and incomplete dehazing in the far view in this scene. Ren's algorithm maintains the far view area well, while the close-up view appears to be oversaturated. Figs.14 and 15 show the comparison results of images of dense hazy and thin hazy scenes.

(a) Hazy image (b) He[3] (c) Wang[5] (d) Yang[6] (e) Sun[15] (f) Li[8] (g) Ren[9] (h) Ours

**Fig. 13 Comparison of results of abrupt changes in scene depth scene images**

(a) Hazy image (b) He[3] (c) Wang[5] (d) Yang[6] (e) Sun[15] (f) Li[8] (g) Ren[9] (h) Ours

**Fig. 14 Comparison of results of dense hazy scene images**

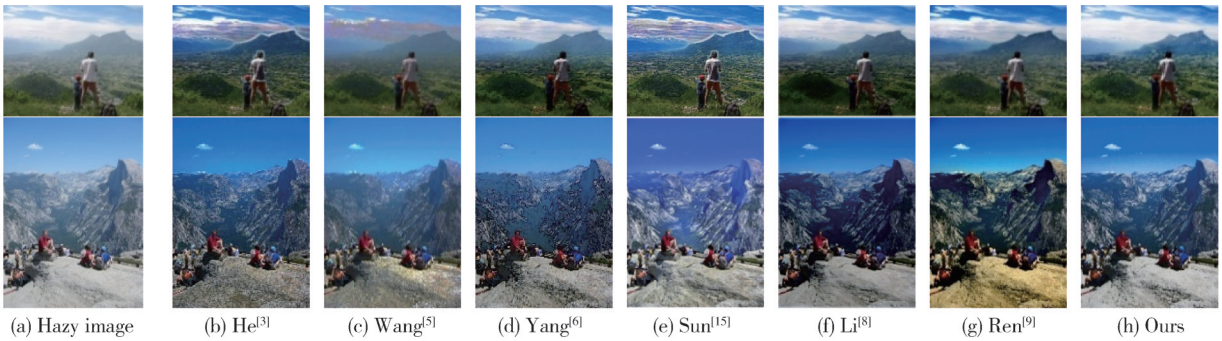

(a) Hazy image (b) He[3] (c) Wang[5] (d) Yang[6] (e) Sun[15] (f) Li[8] (g) Ren[9] (h) Ours

**Fig. 15 Comparison of results of thin hazy scene images**

It can be seen that He's algorithm has a good dehazing effect in the dense hazy scene, and the detail information is kept relatively intact. While in the thin hazy scene, He's algorithm appears to dehaze excessively, resulting in distorted hazy-free images. Wang's algorithm, Yang's algorithm, Sun's algorithm, and Li's algorithm have a

good recovery effect in the thin hazy scene, but the dehazing is not complete in the dense hazy scene. Ren's algorithm has a more stable dehazing effect in both dense hazy and thin hazy scenes, but the recovery results are seriously off-color.

### 3.2 Objective evaluation

The judgment based on subjective evaluation alone is partial, therefore, we verify the objective aspects from the side. The quality assessment method without reference images is used to objectively evaluate Figs.11—15. Visible edge increase rate $v$, average gradient $r$, saturation pixel ratio $\delta$, and runtime $t$ are used as evaluation indexes. Among them, $v$ indicates the degree of edge enhancement of the displayed dehazed image, $r$ represents the ability of the algorithm to recover edge and texture information, $\delta$ denotes the proportion of newly emerging saturation points to the whole image, which can reflect the occurrence of oversaturation in the algorithm, $t$ reflects the running time of the algorithm. The larger the marginal growth rate and average gradient, the better the effect. The smaller the saturated pixel rate, the longer the run time, the better the effect. The formulas are

$$v=\frac{n_r-n_0}{n_0}, \tag{34}$$

$$r=\exp\left(\frac{1}{n_r}\sum_{p_i\in X}\log r_i\right), \tag{35}$$

$$\delta=\frac{n_s}{MN}, \tag{36}$$

where $n_r$ denotes the number of visible edges of the recovered image; $n_0$ is the number of visible edges of the haze image; $r_i$ is the average gradient ratio of the dehazed image to the hazy image at $p_i$; $X$ is the set of visible edges of the dehazed image; $n_s$ denotes the newly emerged saturated pixel point and $MN$ denotes the number of pixels in the whole image.

The experimental data are shown in Fig.16.

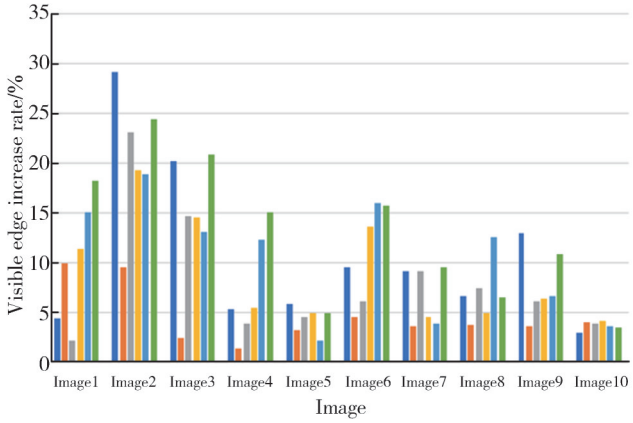


(a) Visible edge increase rate of different images by various methods

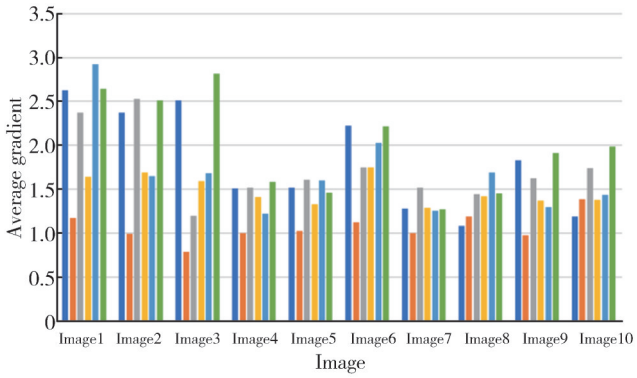


(b) Average gradient of different images by various methods

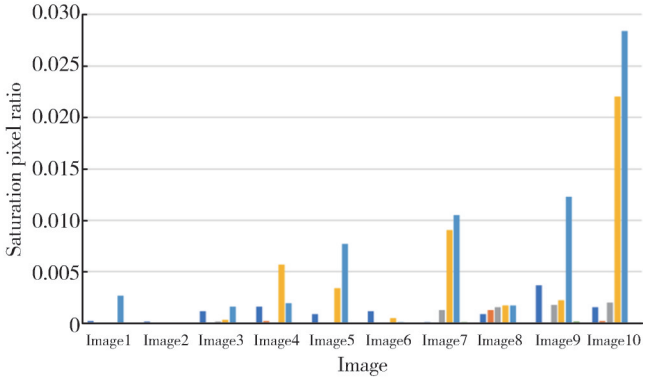


(c) Saturation pixel ratio of different images by various methods

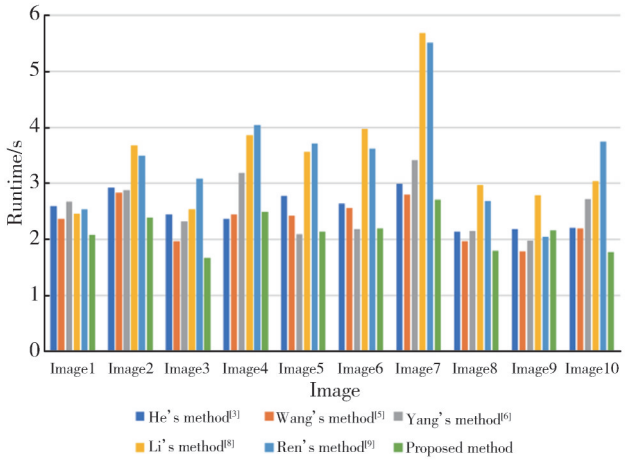


(d) Runtime of different images by various methods

**Fig. 16 Objective evaluation**

It can be seen that the proposed alorithm has achieved good performance in each index. But the visible edge increase rate is slightly less than He's algorithm[3]. For the average gradient, the proposed algorithm is slightly less than Ren's algorithm[9] in the first panel. For the saturated pixel ratio and running time, the proposed algorithm is more advantageous than other algorithms.

### 3.3 Comparative validation of test sets

Since the deep learning algorithm was chosen for the experimental comparison of real hazy images in the subjective and objective evaluation, three synthetic haze

images from the RESIDE synthetic dataset were choser to compare the recovery effects of different algorithms. The outdoor, outdoor with sky, and indoor images are selected respectively for verification. The experimental results are shown in Fig.17.

(a) Hazy image (b) He[3] (c) Wang[5] (d) Yang[6] (e) Sun[15] (f) Li[8] (g) Ren[9] (h) Ours (i) Real image

**Fig. 17 Dehazing effect of different algorithms on RESIDE test set images**

The objective average metrics of the test set are shown in Table 1. The peak signal-to-noise ratio (PSNR) and the structural similarity (SSIM) were used for measurement, both of which are the larger the better. (The data in the table are mean values).

**Table 1 Dataset evaluation metrics**

| Algorithms | PSNR/dB | SSIM |
|---|---|---|
| He[3] | 11.020 | 0.639 |
| Wang[5] | 11.917 | 0.652 |
| Yang[6] | 13.684 | 0.654 |
| Sun[15] | 12.012 | 0.678 |
| Li[8] | 12.598 | 0.858 |
| Ren[9] | 13.179 | 0.724 |
| Ours | 13.740 | 0.873 |

According to Fig.17, it can be seen that whether it is a real hazy image or a synthetic hazy image, the hazy removal effect of the algorithm based on the image restoration is more stable. In addition, the advantages and disadvantages that appear in the real hazy image are also reflected in the synthetic hazy image. While the dehazing algorithm based on deep learning uses the training set of mainly synthetic images, which leads to the good hazy removal effect in the synthetic hazy image and the unstable recovery result in the real hazy image. Table 1 shows that the proposed algorithm also achieves good results in the synthetic hazy images, which verifies the feasibility of the proposed algorithm in dealing with different kinds of hazy images.

## 4 Conclusions

A multi-scale fused opening dark channel (MFODC) was constructed by setting multiple structural element scales. Based on the relationship between image brightness, saturation, scene depth and transmission, a multi-scene adaptive transmission correction model was proposed by analyzing fuzzy images of different scenes experimentally. Optimized local atmospheric light was obtained from local atmospheric light by using brightness information and morphology closing. Then the adaptive correction formula was used to make the requested atmospheric light applicable to different scenes.

## Acknowledgement

This work was supported by National Natural Science Foundation of China (No. 61561030); College Industry Support Plan Project of Gansu Provincial Department of Education (No.2021CYZC-04); Educational Reform Fund of Lanzhou Jiaotong University (No.JG201928).

## Declaration of conflicting interests

The authors have no conflict of interests related to this publication.

## References

[1] TAN R T. Visibility in bad weather from a single image// 2008 IEEE Conference on Computer Vision and Pattern Recognition, June 23-28, 2008, Anchorage, AK, USA. New York: IEEE, 2008: 1-8.

[2] FATTAL R. Single image dehazing. ACM Transactions on Graphics, 2008, 27(3): 1-9.

[3] HE K M, SUN J, TANG X O. Single image haze removal using dark channel prior//2009 IEEE Conference on Computer Vision and Pattern Recognition, June 20-25, 2009, Miami, FL, USA. New York: IEEE, 2009: 1956-1963.

[4] ZHU Q S, MAI J M, SHAO L. A fast single image haze removal algorithm using color attenuation prior. IEEE Transactions on Image Processing: a Publication of the IEEE Signal Processing Society, 2015, 24(11): 3522-3533.

[5] WANG W C, YUAN X H, WU X J, et al. Fast image dehazing method based on linear transformation. IEEE Transactions on Multimedia, 2017, 19(6): 1142-1155.

[6] YANG Y, WANG Z W. Haze removal: push DCP at the edge. IEEE Signal Processing Letters, 2020, 27: 1405-

1409.
[7] LI B Y, PENG X L, WANG Z Y, et al. AOD-net: all-in-one dehazing network//2017 IEEE International Conference on Computer Vision (ICCV), October 22-29, 2017, Venice, Italy. New York: IEEE, 2017: 4780-4788.
[8] LI R, PAN J, HE M, et al. Task-oriented network for image dehazing. IEEE Transactions on Image Processing, 2020, 29: 6523-6534.
[9] REN W Q, LIU S, ZHANG H, et al. Single image dehazing via multi-scale convolutional neural networks. International Journal of Computer Vision. 2020, 128(1): 240-259.
[10] ZHENG Z R, REN W Q, CAO X C, et al. Ultra-high-definition image dehazing via multi-guided bilateral learning//2021 IEEE/CVF Conference on Computer Vision and Pattern Recognition (CVPR), June 20-25, 2021, Nashville, TN, USA. New York: IEEE, 2021: 16180-16189.
[11] LI O, SHUI P L. Noise-robust color edge detection using anisotropic morphological directional derivative matrix. Signal Processing, 2019, 165: 90-103.
[12] LIU X, ZHANG H, TANG Y Y, et al. Scene-adaptive single image dehazing via opening dark channel model. IET Image Processing, 2016, 10(11): 877-884.
[13] SALAZAR-COLORES S, CABAL-YEPEZ E, RAMOS-ARREGUIN J M, et al. A fast image dehazing algorithm using morphological reconstruction. IEEE Transactions on Image Processing, 2019, 28(5): 2357-2366.
[14] JIN X L, ZHANG W, LIU L F. Image defogging algorithm based on guided filtering and adaptive tolerance. Journal on Communications, 2020, 41(5): 27-36.
[15] SUN W, WANG H, SUN C H, et al. Fast single image haze removal via local atmospheric light veil estimation. Computers & Electrical Engineering, 2015, 46: 371-383.
[16] YANG Y, ZHANG H W, ZHANG J L. Single image dehazing combining sky segmentation and transmission mapping. Optics and Precision Engineering, 2021, 29(2): 400-410.
[17] SHEN Y Y, LIU C X, ZHANG J D, et al. Atmospheric light correction and transmission optimization based robust image dehazing. Journal of Computer-Aided Design & Computer Graphics, 2017, 29(9): 1604-1612.
[18] LÜ J W, QIAN F, HAN H N, et al. Nighttime image dehazing with a new light segmentation method and a linear image depth estimation model. Chinese Optics, 2022, 15(1): 34-44.
[19] LI B Y, REN W Q, FU D P, et al. Benchmarking single-image dehazing and beyond. IEEE Transactions on Image Processing, 2019, 28(1): 492-505.
[20] ZHAO X. Single image dehazing using bounded channel difference prior//IEEE/CVF Conference on Computer Vision and Pattern Recognition Workshops, June 19-25, 2021, Nashville, TN, USA. New York: IEEE, 2021, 727-735.

# 多尺度形态学下的自适应透射率修正去雾算法

张　帅，杨　燕*

兰州交通大学 电子与信息工程学院，甘肃 兰州 730070

**摘　要：**针对图像去雾中由于透射率与大气光估计不准，导致复原结果偏色、出现视觉偏差等问题，本文提出一种基于多尺度形态学重构的自适应透射率与大气光修正的去雾算法。首先，该算法利用形态学重构下的开运算操作代替暗通道中最小值滤波操作，并利用图像形态学边缘设定开运算结构元素尺度，构造一种多尺度的开运算融合暗通道。并经过形态学消噪处理后，得到精确初始透射率。对于含天空雾图暗通道失效的问题，依照雾图中亮度和饱和度差异与透射率的关系，结合高斯函数拟合一种自适应透射率修正模型，对含天空雾图的初始透射率进行修正。然后，根据图像亮度信息与形态学闭运算改进局部大气光。最后，结合所提算法与大气散射模型获得准确的无雾图像。实验结果表明，本文所提算法适用于多种场景下的雾图复原，且复原效果良好，明亮度适宜。

**关键词：**图像去雾；形态学重构；多尺度融合暗通道；自适应修正；多场景复原

**引用格式：**ZHANG Shuai, YANG Yan. Dehazing algorithm for adaptively corrected transmission under multi-scale morphology. Journal of Measurement Science and Instrumentation, 2024, 15(4): 477-489.